

## SOUTHERN COSMOLOGY SURVEY I: OPTICAL CLUSTER DETECTIONS AND PREDICTIONS FOR THE SOUTHERN COMMON-AREA MILLIMETER-WAVE EXPERIMENTS

FELIPE MENANTEAU<sup>1</sup>, JOHN P. HUGHES<sup>1</sup>, RAUL JIMENEZ<sup>2,3</sup>, CARLOS HERNANDEZ-MONTEAGUDO<sup>4</sup>, LICIA VERDE<sup>2,3</sup>, ARTHUR KOSOWSKY<sup>5</sup>, KAVILAN MOODLEY<sup>6</sup>, LEOPOLDO INFANTE<sup>7</sup> AND NATHAN ROCHE<sup>8</sup>

*Accepted for publication in ApJ*

### ABSTRACT

We present first results from the Southern Cosmology Survey, a new multiwavelength survey of the southern sky coordinated with the Atacama Cosmology Telescope (ACT), a recently commissioned ground-based mm-band Cosmic Microwave Background experiment. This article presents a full analysis of archival optical multi-band imaging data covering an 8 square degree region near right ascension 23 hours and declination -55 degrees, obtained by the Blanco 4-m telescope and Mosaic-II camera in late 2005. We describe the pipeline we have developed to process this large data volume, obtain accurate photometric redshifts, and detect optical clusters. Our cluster finding process uses the combination of a matched spatial filter, photometric redshift probability distributions and richness estimation. We present photometric redshifts, richness estimates, luminosities, and masses for 8 new optically-selected clusters with mass greater than  $3 \times 10^{14} M_{\odot}$  at redshifts out to 0.7. We also present estimates for the expected Sunyaev-Zel'dovich effect (SZE) signal from these clusters as specific predictions for upcoming observations by ACT, the South Pole Telescope and Atacama Pathfinder Experiment.

*Subject headings:* cosmic microwave background — cosmology: observations — galaxies: distances and redshifts — galaxies: clusters: general — large-scale structure of universe — methods: data analysis

### 1. INTRODUCTION

The new generation of high-angular resolution Cosmic Microwave Background (CMB) ground-based experiments represented by the the Atacama Cosmology Telescope (ACT) (Kosowsky 2006; Fowler et al. 2007) and the South Pole Telescope (SPT) (Ruhl et al. 2004) are currently targeting their observations in a common area in the southern sky that will ultimately cover several hundreds to thousands of square degrees. These experiments will provide a blind survey of the oldest light in the Universe at wavelengths of 1 – 2 mm and angular scales beyond the resolution limits of the WMAP and Planck satellites. At these arcminute angular scales, temperature fluctuations in the CMB are dominated by secondary effects arising from the formation of large-scale structure in the universe. One of the strongest effects is the imprint left by galaxy clusters through the Sunyaev Zel'dovich effect (SZE) (Sunyaev & Zeldovich 1980) in which CMB photons suffer inverse Compton scattering by the hot intracluster gas. ACT and SPT are designed

to detect the SZE, through its frequency-dependence: these experiments will measure temperature shifts of the CMB radiation corresponding to a decrement below and an increment above the “null” frequency around 220 GHz.

Much can be learned about the Universe from these surveys. First, accurate systematics-free maps will allow measurement of the primary power spectrum of temperature fluctuations at all scales on which they are the dominant contribution. Second, these data sets will result in a complete census of massive clusters to arbitrarily large distances, limited only by a minimum cluster mass set largely by the instrumental sensitivity and expected to be several  $10^{14} M_{\odot}$  (Ruhl et al. 2004; Sehgal et al. 2007). Thanks to the relatively clean selection function as well as the redshift independence of the SZE, the cluster sample, especially the evolution of the number density of clusters with redshift, will be quite sensitive to the growth of structure in the Universe offering a potentially powerful probe of dark energy (Carlstrom et al. 2002). Moreover, the SZE data in combination with optical, UV and X-ray observations can teach us a great deal about the detailed physics of cluster atmospheres and galaxy evolution in these dense environments.

Significant observing time and effort has been devoted to the development of techniques and the detection of galaxy clusters using large-area optical catalogs and X-ray observations. Several projects have taken advantage of large-area CCD imaging and have developed automated cluster detection schemes to produce large catalogs of clusters of galaxies (see Koester et al. 2007; Postman et al. 1996, 2001; Gal et al. 2000, 2003, 2009; Gladders & Yee 2005, for example) which target the relative over-abundance of galaxies over a range of redshifts. Similarly, X-ray surveys such as the *ROSAT* All Sky Survey

<sup>1</sup> Rutgers University, Department of Physics & Astronomy, 136 Frelinghuysen Rd, Piscataway, NJ 08854, USA

<sup>2</sup> ICREA & Institute of Space Sciences (CSIC-IEEC), Campus UAB, Bellaterra, Spain

<sup>3</sup> Department of Astrophysical Sciences, Peyton Hall, Princeton University, Princeton, NJ 08544, USA

<sup>4</sup> Max Planck Institut für Astrophysik, Karl Schwarzschild Str.1,D-85741, Garching Munchen, Germany

<sup>5</sup> University of Pittsburgh, Physics & Astronomy Department, 100 Allen Hall, 3941 O'Hara Street, Pittsburgh, PA 15260, USA

<sup>6</sup> University of KwaZulu-Natal, Astrophysics & Cosmology Research Unit, School of Mathematical Sciences, Durban, 4041, South Africa.

<sup>7</sup> Pontificia Universidad Católica de Chile, Departamento de Astronomía, Santiago, Chile

<sup>8</sup> University of Pennsylvania, Physics and Astronomy, 209 South 33rd Street, Philadelphia, PA 19104, USA

(Ebeling et al. 1998; Böhringer et al. 2001; Mullis et al. 2003) produced catalogs with hundreds of galaxy clusters, while pointed X-ray observations have discovered systems up to  $z \simeq 1.4$  (Mullis et al. 2005).

With this article we inaugurate the Southern Cosmology Survey (SCS). This project, funded by the National Science Foundation under the Partnership in Research and Education (PIRE) program, is a multiwavelength (radio, mm-band, optical, UV, and X-ray) large area survey specifically coordinated with ACT observations of the southern sky. The goal of the SCS is to maximize the scientific return from the new ground-based CMB experiments and therefore focuses on specific observational studies relevant to this science, such as the selection function of galaxy clusters across wavebands, cluster mass determination, and the establishment a "gold" sample of clusters for cosmology and galaxy evolution studies. Here we present results from an  $\simeq 8 \text{ deg}^2$  optical imaging survey of the southern sky that overlaps the common SZ survey region. The purpose of this paper is twofold: (1) to present the details of our data reduction pipeline and analysis software and (2) identify new galaxy clusters, constrain their redshifts and masses, and predict their SZ signals. Photometric redshifts come from the 4-band imaging data, while our mass estimates are inferred from the optical luminosity ( $L_{200}$ ) and richness ( $N_{200}^{\text{gal}}$ ) of the clusters, using relations calibrated by the Sloan Digital Sky Survey (SDSS). For the eight massive clusters, out of 38 identified (37 are new sources) in the survey area, we present positions, richness estimates, masses, and predictions for the integrated Compton  $y$ -distortion of the SZE using empirical power-law relations based on  $N$ -body simulations. Throughout this paper we assume a flat cosmology with  $H_0 = 100h \text{ km s}^{-1} \text{ Mpc}^{-1}$ ,  $h = 0.7$  and matter density  $\Omega_m = 0.3$ .

## 2. DATASET AND METHODOLOGY

Our study is based on the optical multi-band analysis of public data from the Blanco Cosmology Survey<sup>9</sup> (BCS). This is a NOAO Large Survey Project that was awarded 45 nights over three years on the Blanco 4-m telescope at the Cerro Tololo InterAmerican Observatory (CTIO). The survey aims to image two 50 square-degree patches of the southern sky in four optical bands ( $griz$ ) using the  $8192 \times 8192$  pixel ( $0.36 \text{ deg}^2$ ) MOSAIC II camera in order to attain a sensitivity about an order of magnitude deeper than the SDSS imaging. The targeted areas are centered near declinations of  $-55^\circ$  and  $-52^\circ$  at right ascensions of 23 hr and 5 hr respectively; each of these patches lies within a larger common region of the southern sky that both ACT and SPT plan to survey. The BCS began in 2005 and has completed three years of data taking. For this paper we have processed and analyzed public data from the first year of the survey using an independent software pipeline developed by us at Rutgers University. The data we present was obtained on 15 nights of observing near the end of November and the beginning of December 2005 and cover an area of  $\simeq 8 \text{ deg}^2$  in the 23 hr region. In Table 1 we show the observing dates, photometric conditions, lunar illumination and observed bands for the 19 tiles that make up the full extent of the observations analyzed here. In the follow-

TABLE 1  
2005 OBSERVATIONS IN THE 23HR FIELD

Date	Photometric	Lunar Illum	# of Tiles Obs			
			$g$	$r$	$i$	$z$
18 Nov 2005	yes	89.4%	1.0	1.0	3.0	3.0
19 Nov 2005	yes	0.0%	4.5	4.5	1.0	1.0
20 Nov 2005	no	0.0%	8.0	8.0	0.0	0.0
22 Nov 2005	no	0.0%	0.0	0.0	0.0	0.0
24 Nov 2005	yes	0.0%	2.0	2.0	0.0	0.0
26 Nov 2005	yes	0.0%	3.0	3.0	1.0	1.0
28 Nov 2005	yes	0.0%	0.0	0.0	2.7	2.7
30 Nov 2005	yes	0.0%	0.0	0.0	0.3	0.3
02 Dec 2005	yes	0.0%	0.5	0.5	0.0	0.0
04 Dec 2005	no	15.3%	0.0	0.0	0.0	0.0
05 Dec 2005	no	24.5%	0.0	0.0	1.3	1.7
06 Dec 2005	yes	35.1%	0.0	0.0	1.3	1.0
08 Dec 2005	yes	57.8%	0.0	0.0	2.3	2.7
10 Dec 2005	yes	78.4%	0.0	0.0	3.0	3.0
11 Dec 2005	yes	86.6%	0.0	0.0	3.0	3.3

NOTE. — Observing conditions during the 2005 run of the BCS, consisting of only the 19 tiles that were fully observed in all 4 bands in the 23hr region. Lunar illumination is the percentage at midnight local time in the direction toward the center of the region surveyed (R.A. 23 hours, decl.  $-55.2\text{deg}$ ).

ing we describe the steps followed and tasks performed by the pipeline.

### 2.1. The Rutgers Southern Cosmology Pipeline

The Rutgers Southern Cosmology image analysis pipeline is written in Python with a scalable object-oriented design based on existing public astronomical software that is aimed at processing a large dataset in a repeatable, stable and semi-automated fashion.

The initial standard image processing steps for each observing night are handled by the IRAF/mscred (Valdes 1998) procedures via the STScI/Pyraf interface. These include: overscan trim, bias correction, CCD cross-talk coefficients corrections as well as dome flat field correction. The pipeline also executes secondary CCD calibration steps on the science images which include the creation of super sky-flats, fringe patterns for  $i$ - and  $z$ -bands and their corresponding correction and removal. Additionally, procedures affecting the cosmetic appearance of the images, such as cosmic ray rejection, removal of saturated star bleed-trails, and generation of bad pixel masks, are automatically performed at this stage. Astrometric re-calibration and WCS plate solution are also handled automatically at this stage on the pre-stack science images using IRAF's mscred/mscmatch task by matching several hundred sources within each tile with stars from the US Naval Observatory Catalog. We achieve good accurate astrometric solutions (the residual error in matched source positions was typically  $< 0.1''$ ) as tested using the overlapping regions between neighboring pointings. Photometric standard star fields were processed together with the normal science images and photometric zero points for each observing night were obtained using a few hundred standards from the Southern Hemisphere Standards Stars Catalog (Smith et al. 2007). Like these authors we use the AB magnitude system.

The survey strategy followed a predetermined observing pattern, which typically consisted of exposures of

<sup>9</sup> <http://cosmology.uiuc.edu/BCS/>

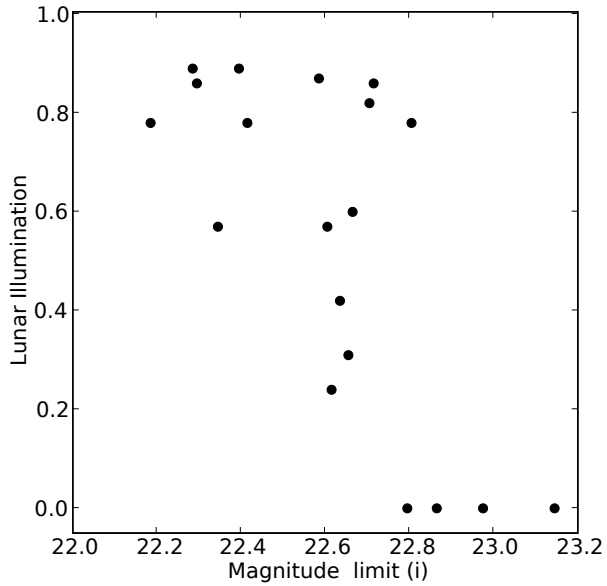


FIG. 1.— The mean lunar illumination fraction for each tile at time of observation in the 23hr field as a function of the  $i$ -band magnitude limit for 90% completeness.

$2 \times 125s$ ,  $2 \times 300s$ ,  $3 \times 450s$  and  $3 \times 235s$  in the  $g$ ,  $r$ ,  $i$  and  $z$ -bands respectively with offsets of 3 – 5 arcmin (within each filter) intended to provide significant overlap between neighboring MOSAIC II tiles and fill in the gaps between CCDs chips. We used the overlapping regions between tiles to adjust the photometric zero points of non-photometric nights using matched sources from adjacent photometric tiles. This ensured a homogeneous photometric calibration across the full survey region with typical variations below 0.02 mags.

Image alignment, stacking and combination as well as catalog generation are performed at a secondary stage by the pipeline using association files, which describes a logical group of exposures and filters, created for each tile. Science images were mosaiced, aligned and median combined using SWarp (Bertin 2006) to a plate scale of  $0.266''/\text{pixel}$ . Source detection and photometry measurements for the science catalogs were performed using SExtractor (Bertin & Arnouts 1996) in dual-image mode in which sources were identified on the  $i$ -band images using a  $1.5\sigma$  detection threshold, while magnitudes were extracted at matching locations from all 4 bands.

As our data set is composed of observations taken over several weeks under varying conditions during the 2005 campaign, we determined, for each tile individually, the  $i$ -band magnitude limit at which the galaxy detection limit was complete to 90%. To compute this limit we use the fact that the galaxy number counts follow a power-law function, which we fitted in the magnitude range  $19.5 < i < 21.5$  in each tile and extrapolated to obtain the magnitude at which the galaxy number counts dropped by 10%. We took this as the 90% completeness limit for the tile. We found variations of roughly 1 magnitude on the limits among the 19 tiles and, in an attempt to understand this, we investigated a possible correlation with lunar illumination at the time of obser-

vation. Figure 1 shows a clear trend between the  $i$ -band magnitude limit and the lunar illumination. We report a mean limit  $i = 22.62 \pm 0.25$  and we set a conservative magnitude limit of  $i = 22.5$  for our full catalog.

## 2.2. Photometric Redshifts

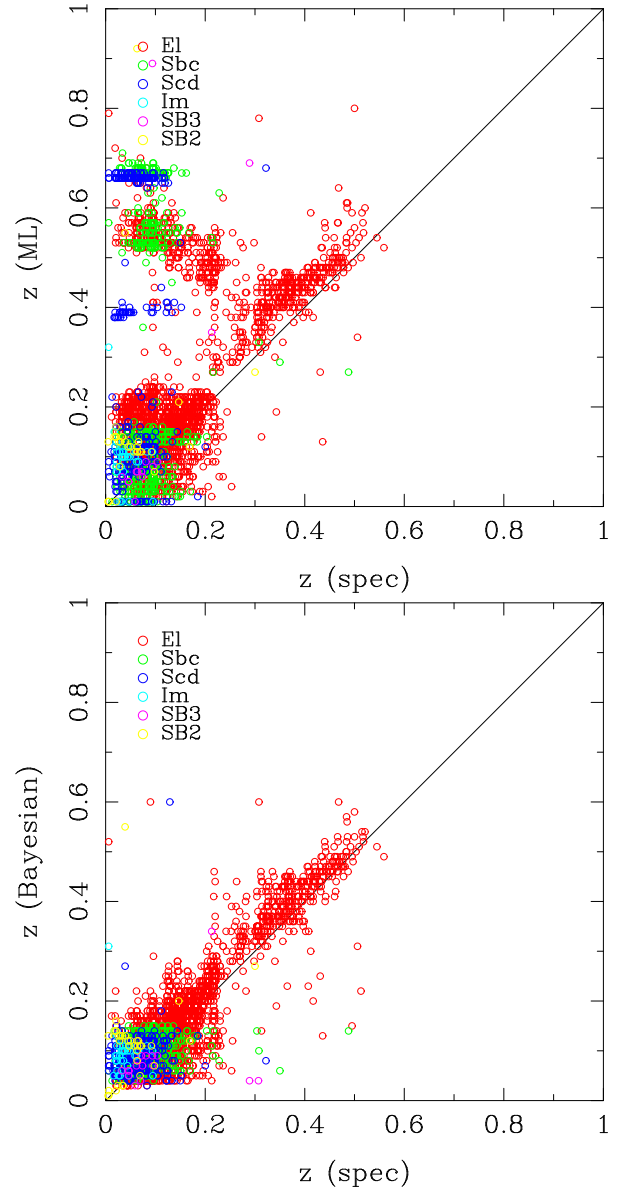


FIG. 2.— Comparison between photometric and spectroscopic redshifts for 5000 galaxies in the SDSS DR6. The upper panel shows the comparison between spectroscopic and photometric redshifts obtained under the maximum likelihood assumption. The lower panel uses a Bayesian assumption with a custom empirical prior on galaxy brightness for the photometric redshifts. Symbols are color coded according to the best determined SED by BPZ. SEDs for E/S0 galaxies tend to dominate at higher redshifts as the SDSS is biased towards early-type galaxies which are the most luminous population at these redshifts.

From the multi-band photometry the pipeline computes photometric redshifts and redshift probability distributions  $p_{\text{BPZ}}(z)$  for each object using the  $g$ ,  $r$ ,  $i$ ,  $z$  isophotal magnitudes, as defined by the  $i$ -band detection, and the BPZ code (Benítez 2000). We use a magnitude-based empirical prior (Benitez, private communication)

taken from the SDSS and HDF-N spectroscopic redshift distributions, which accounts for the tendency of fainter galaxies to be more likely found at higher redshifts (See Fig 4. from Benítez 2000, as an example). Because the area covered by the available NOAO imaging does not include any publicly available spectroscopic redshift information for  $z > 0.1$  (NASA/IPAC Extragalactic Database, NED), we investigated the accuracy of our photometric redshift estimates using ancillary data. As the ability of BPZ to estimate photometric redshifts at fainter magnitudes ( $i > 20$ ) from multi-band photometry has been consistently established in the past using filter sets similar to ours here (Benítez et al. 2004; Mobasher et al. 2004; Cross et al. 2004, for example), we focused on the redshift accuracy at  $z < 0.5$ . To this end we extracted  $g, r, i, z$  photometry from the DR6 SDSS for 5000 randomly-selected bright galaxies ( $r < 20$  mag) with reliable spectroscopic redshifts, matching the depth and signal-to-noise ratio of our galaxy sample. We computed photometric redshifts for the SDSS spectroscopic sample in the same way as just described and compared the resulting values to the spectroscopic redshifts. We found, not surprisingly, that simply employing the maximum-likelihood (ML) condition is an ill-suited approach for redshifts below  $z < 0.3$  in the absence of a bandpass bluer than  $3000\text{\AA}$  as it largely over-estimates redshifts and produces an unacceptable number of catastrophic outliers. Recently, Niemack et al. (2008) have demonstrated how the addition of bluer bands using GALEX UV imaging greatly improves ML estimates and reduces the need for priors. On the other hand, Bayesian estimates give results with typical rms errors of  $\delta z \sim 0.02$  and with almost no catastrophic outliers. In Fig. 2 we show the results of our comparison between ML and Bayesian photometric versus spectroscopic redshifts color-coded according to the spectral energy distribution (SED) determined by the BPZ code. It is clear from the figure that at higher redshifts the SDSS population is dominated by early types as these tend to be the most luminous objects. We also note (see fig. 2, lower panel) that on average our photometric redshifts tend to overpredict the true redshifts. The mean bias level  $\langle z_{\text{spec}} - z_{\text{BPZ}} \rangle$  for galaxies with E/S0s SEDs is largest around  $z_{\text{spec}} \sim 0.3$  where it is on the order of  $\delta z \sim -0.03$ . In table 2 we show the mean bias and standard deviation for three redshift intervals for  $z_{\text{spec}} - z_{\text{BPZ}}$  as well as the standard  $dz$  defined as  $dz = z_{\text{spec}} - z_{\text{BPZ}} / (1 + z_{\text{spec}})$ . In summary we are able to determine the redshifts for early-type galaxies to an accuracy better than 0.1 across the redshift range of the survey. This is encouraging since early-type galaxies are the predominant population in clusters of galaxies and good photometric redshift determination is essential for successful cluster finding, as we discuss in the next section.

In Figure 3 we show the photometric redshift distribution for all galaxies within our flux completeness limit,  $i < 22.5$ , as well as the filter responses for the survey<sup>10</sup>. Our distribution peaks around  $z \sim 0.6$ , which sets a conservative upper limit to the redshift at which we are able to detect optical clusters.

### 2.3. Computing Overdensities and Finding Clusters

<sup>10</sup> <http://www.ctio.noao.edu/instruments/FILTERS/index.html>

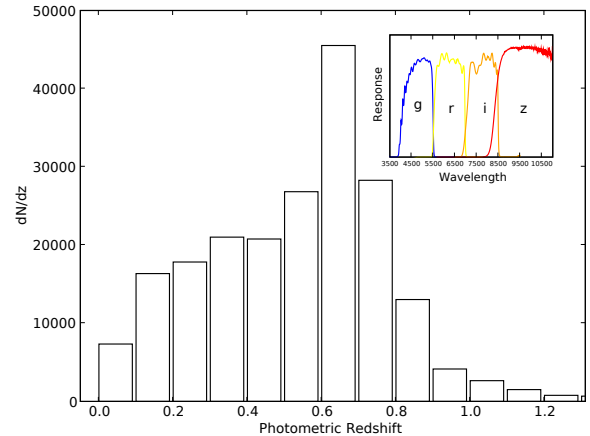


FIG. 3.— The photometric redshift distribution of the galaxy sample used for finding clusters (i.e.: galaxies  $i < 22.5$  mag).

TABLE 2  
PHOTOMETRIC REDSHIFT SIMULATIONS STATISTICS

Redshift	$\langle z_{\text{spec}} - z_{\text{BPZ}} \rangle$	$(z_{\text{spec}} - z_{\text{BPZ}})_{\text{rms}}$	$\langle dz \rangle$	$\sigma_z$
0.0 – 0.2	-0.017	0.042	-0.015	0.038
0.2 – 0.4	-0.027	0.059	-0.020	0.047
0.4 – 0.6	-0.002	0.070	-0.001	0.048

NOTE. — The mean difference and standard deviation between spectroscopic and recovered photometric redshifts as well as for  $dz$  for all galaxies with SED determined to be E/S0s in three redshift ranges.

One of the main goals of the current SZE experiments is to define a mass-selected sample of galaxy clusters out to large redshifts. At long last this is beginning to happen (Staniszewski et al. 2008; Menanteau & Hughes 2009), after a number of successful individual detections of the SZE in well-known optical or x-ray clusters (see Birkinshaw et al. 1991; Jones et al. 1993; Herbig et al. 1995; Reese et al. 2000; Gómez et al. 2003; Bonamente et al. 2006; Halverson et al. 2008, and references therein). If we want to understand the systematics of SZE surveys it is crucial to compare with cluster identifications using independent methods. In this section, we describe our effort to select clusters of galaxies from multi-wavelength optical imaging. There are several methodologies and a plethora of papers describing these techniques (Postman et al. 1996; Gladders & Yee 2005; Koester et al. 2007; Eisenhardt et al. 2008, for example) but they all rely on the same well-known properties of galaxy clusters: a) early-type galaxies are the dominant population, b) cluster galaxies have very similar colors, and display tight color-magnitude relationships across several orders of magnitude in luminosity, and c) the surface number density of cluster galaxies falls off with distance from the center roughly as a power law  $P(r) \propto 1/r^\alpha$ . We search for clusters using a matched filter approach similar to the one described in Postman et al. (1996) and then define membership and estimate richness of the clusters using the MaxBCG prescription (Koester et al. 2007).

Our cluster finder method folds in the contributions

from a cluster spatial profile filter function  $P(r)$ , a luminosity weight  $L(m)$  and the BPZ redshift probability distribution  $p_{\text{BPZ}}(z)$  from each source to generate likelihood density maps (at pixel positions denoted by  $i, j$ ) or a “filtered” galaxy catalog  $S(i, j)(z)$  over the area covered by the survey as a function of redshift, namely,

$$S(i, j)(z) = \sum_{k=1}^{N_g} P(r_k[i, j]) L(m_k) \int_{z-\Delta z}^{z+\Delta z} p_{\text{BPZ}}(z_k) dz. \quad (1)$$

Specifically we use a profile with the form

$$P(r/r_c) = \frac{1}{\sqrt{1 + (r/r_c)^2}} - \frac{1}{\sqrt{1 + (r_{\text{cut}}/r_c)^2}}, \text{ if } r < r_{\text{cut}} \\ = 0, \text{ otherwise} \quad (2)$$

which is normalized as

$$\int_0^\infty P(r/r_c) 2\pi r dr = 1 \quad (3)$$

and where  $r_c$  is the typical cluster core radius and  $r_{\text{cut}}$  is the cutoff limit for the function. In our analysis we chose  $r_c = 175$  kpc and  $r_{\text{cut}} = 10r_c$ . We also use a luminosity weight  $L(m)$  given by

$$L(m) = \frac{\phi(m - m^*) 10^{-0.4(m - m^*)}}{b(m)} = \frac{\Phi(m - m^*)}{b(m)} \quad (4)$$

where  $m^*$  is the apparent magnitude corresponding to  $M^*$ . This function is normalized as

$$\int_0^{m_{\text{lim}}} \Phi(m - m^*) dm = 1 \quad (5)$$

where  $m_{\text{lim}}$  is the flux limit of the sample ( $i = 22.5$ ),  $b(m)$  is the number of background galaxies and  $\phi(m)$  is the Schechter (1976) galaxy luminosity function. We use the parameters computed from Brown et al. (2007) for the evolving luminosity function of red galaxies, with a faint-end slope  $\alpha = -0.5$  and  $M^*(z)$  between  $0 < z < 1$ . For our estimation of  $b(m)$  we use the number counts from Yasuda et al. (2001). We generate likelihood density maps with a constant pixel scale of 1.2 arcmin at  $\Delta z = 0.1$  intervals between  $0.1 < z < 0.8$  over the surveyed regions. In Figure 4 we show an example of a likelihood density map centered at  $z = 0.2$  on which we superpose outlines of the 19 tiles that define the region studied here.

Cluster candidates are selected from the peaks of the likelihood density maps. In order to define peaks consistently we constructed noise maps by randomizing the positions of the input catalog to produce likelihood density maps following exactly the same procedure as described above. These maps represent the noise floor level above which we desire to detect clusters. We define our initial list of cluster candidates from  $2\sigma$  peaks in the likelihood density maps, where  $\sigma$  is defined as the median value in the noise maps. Cluster candidates were checked for multiple detection in different likelihood maps. To avoid duplication we considered a system unique if detected in two adjacent redshift maps and with the same center (i.e., within  $3'$ ).

#### 2.4. Contamination and Completeness

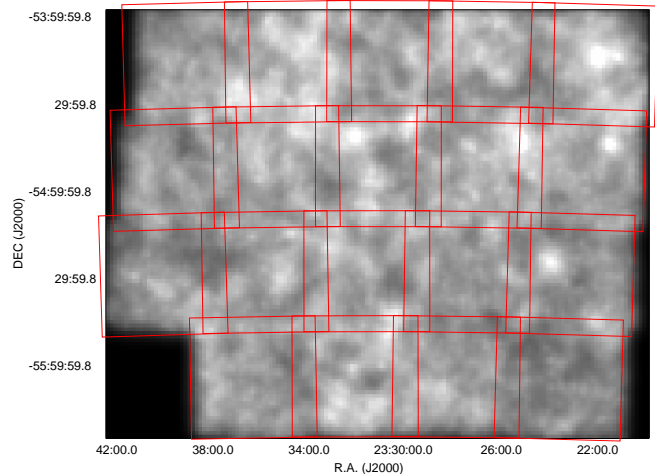


FIG. 4.— The computed likelihood density map image centered at  $z = 0.2$  and width  $\Delta z = 0.1$  over the 23hr field. Bright regions in the image represent denser areas. The red lines represent the area covered by each of the 19 tiles that comprise the area studied.

We performed simulations to investigate our cluster selection function by estimating the contamination and recovery rates of our cluster finding technique. The lack of distance information in imaging surveys is the principal source of contamination as fluctuations in the projected two-dimensional galaxy distribution as well as random alignments of poor groups may result in false apparent overdensities. We explore this issue following the same methodology as used by Postman et al. (2002) and Gal et al. (2003) which rely on generating Monte Carlo representations of the galaxy sample with an angular two-point correlation function similar to that observed (Infante 1994). As described in Postman et al. (2002) we implemented the Rayleigh-Lévy (RL) random walk process using Mandelbrot’s (1975) elegant fractal prescription to simulate galaxy positions on the sky, such that galaxy pairs are placed in a randomly chosen direction at distance  $\theta$  drawn from the distribution:

$$P(> \theta) = \begin{cases} (\theta/\theta_0)^{-d}, & \text{if } \theta \geq \theta_0 \\ 1, & \text{if } \theta < \theta_0, \end{cases} \quad (6)$$

where we chose  $\theta_0$  and  $d$  to match the observed galaxy distribution of our sample. In practice we generate simulated distributions by starting from a randomly selected location within the survey boundaries and generate positions following the RL random walk allowing up to seven galaxies to be drawn around this location. We then select a new center randomly and the process is repeated until we generate the same number of galaxies as in the observed sample. We then process the RL distribution to generate likelihood maps using the same procedure and parameters as for the real data and use these to investigate the rate of false detections as a function of estimated redshift. Since the RL distributions by construction do not explicitly include clusters, we assess the false positive cluster detection fraction by taking the ratio of detections in the simulations per area unit to the observed number of candidates in the real data. We find that at low redshift the false positive fraction is zero (there is virtually no contamination), while at redshifts of  $z = 0.6$  and  $z = 0.7$  the false positive fraction grows to values of

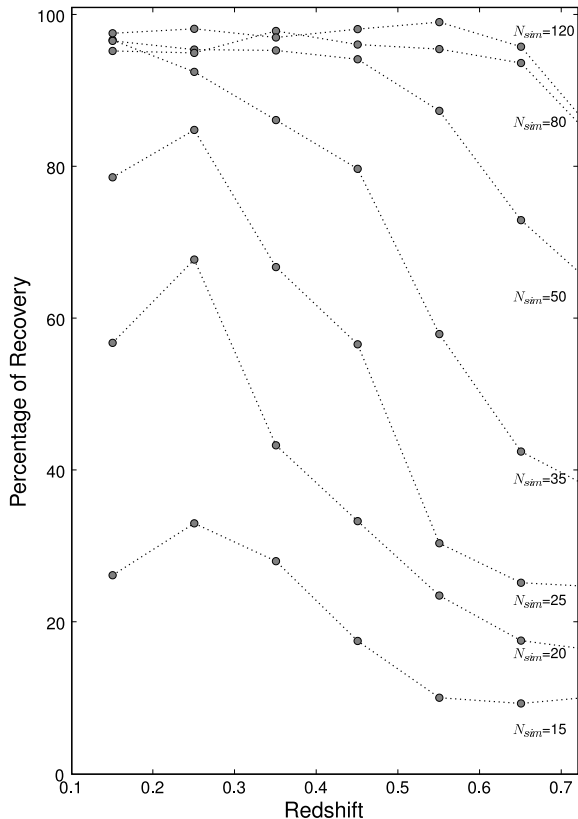


FIG. 5.— The cluster recovery fraction as a function of redshift as extracted from the simulations for clusters with  $N_{sim} = 15, 20, 25, 35, 50, 80$  and  $120$  galaxies and a profile with slope  $\alpha = 1.8$  and core radius  $0.150$  Mpc.

1% and 19%, respectively. We conclude that false positives are not an important source of spurious detections.

We investigate the selection function for our galaxy sample by simulating galaxy clusters of various richness and shapes at different redshifts and examining their recovery fractions. Specifically we generated clusters with random ellipticities uniformly between  $0.1 < z < 0.7$  using an  $r^{-\alpha}$  profile for the galaxy distribution (Lubin & Postman 1996) with  $\alpha = 1.8$  and  $r_c = 0.150$  Mpc and using the luminosity function for red galaxies from Brown et al. (2007). These clusters are inserted 20 at a time in the observed catalogs at random positions and redshifts, but avoiding the locations where clusters were detected. In total we generate 10,000 simulated clusters with richness values,  $N_{sim}$ , of 15, 20, 25, 35, 50, 80 and 120 galaxies uniformly distributed in redshift.<sup>11</sup> We process each realization using the same parameters as for the observed data and record the number of clusters recovered as a function of redshift and galaxy richness. In Figure 5 we show the results of this exercise where we plot the recovery fraction as a function of redshift for the seven cluster richnesses simulated. We conclude that for the rich clusters  $N_{sim} > 50$  we are always nearly complete (80 – 90%) for  $z \leq 0.6$  while for poorer clusters we only detect at best  $\sim 30\%$  around  $z = 0.3$ .

<sup>11</sup> These richness values fold in the flux limit of the survey and the membership prescription as described in the next section, so that they are roughly comparable to the  $N_{gal}$  values we give for the detected clusters.

### 3. CLUSTER PROPERTIES

One of our main drivers in searching for clusters at optical wavelengths is to correlate them with SZ detections in the new blind SZ surveys. The signal to be detected in the mm-band experiments (i.e., the  $y$ -distortion due to inverse Compton scattering) is related to the number of hot electrons in the intracluster medium, and simulations have shown (see Motl et al. 2005; Nagai 2006; Sehgal et al. 2007; Bhattacharya et al. 2007, for example) that the SZE signal is closely linked to cluster mass. Our analysis of the optical survey has provided positions, redshifts, and fluxes of galaxies, from which we infer the underlying cluster mass using scaling relations established by the SDSS, where cluster masses were determined from weak lensing.

#### 3.1. Defining Cluster Membership

The current state-of-the-art mass tracers for clusters of galaxies using optically observed parameters (Johnston et al. 2007; Reyes et al. 2008) have been extracted from a sample of around 13,000 optically-selected clusters from the SDSS MaxBCG catalog (Koester et al. 2007). In this paper, we apply these scaling relations to our cluster sample and obtain mass estimates from which we additionally predict SZ distortions. To be fully consistent with previous analyses, we define membership and all other relevant cluster observables following the same method as Reyes et al. (2008) and Koester et al. (2007).

We begin by examining each candidate-cluster peak in the density maps and select the brightest elliptical galaxy in the cluster (BCG), which is taken to be the initial center and redshift  $z_o$  of the system. We then use galaxies defined as E or E/S0s (i.e., BPZ SED types 0 and 1 only) within a projected radius of  $0.5h^{-1}$  Mpc and redshift interval  $|z - z_o| = |\Delta z| = 0.05$  to obtain a local color-magnitude relation (CMR) for each color combination,  $g - r$ ,  $r - i$  and  $i - z$ , and the cluster mean redshift,  $z_c$ , for all cluster members, using a  $3\sigma$  median sigma-clipping algorithm. We use these to determine  $N_{1\text{Mpc}}$ , the number of galaxies within  $1h^{-1}$  Mpc of the cluster center. Formally, we compute  $N_{gal} = N_{1\text{Mpc}}$  by including those galaxies within a projected  $1h^{-1}$  Mpc from the cluster center that satisfy three conditions: (a) the galaxy must have the SED of an E, E/S0 according to BPZ, (b) it must have the appropriate color to be a cluster member (i.e., colors within  $3\sigma$  of the local CMR for all color combinations) and (c) it must have the right luminosity (i.e., dimmer than the BCG and brighter than  $0.4L^*$ , where we use the corresponding absolute magnitude  $M_i^*$  from Brown et al. (2007) redshifted with the elliptical SED template from BPZ). We designated cluster members according to the estimated cluster size  $R_{200}$ , defined as the radius at which the cluster galaxy density is  $200\Omega_m^{-1}$  times the mean space density of galaxies in the present Universe. We estimated the scaled radius  $R_{200}$  using the empirical relation from Hansen et al. (2005),  $R_{200} = 0.156N_{1\text{Mpc}}^{0.6}h^{-1}$  Mpc which is derived from the SDSS and we assume it holds beyond  $z \sim 0.3$  for our higher redshift clusters.

In our analysis we use  $N_{200}^{\text{gal}}$ ,  $L_{200}$ , and  $L_{\text{BCG}}$  to scale cluster optical parameters with mass, following Reyes et al. (2008). The cluster richness,  $N_{200}^{\text{gal}}$ , is the number

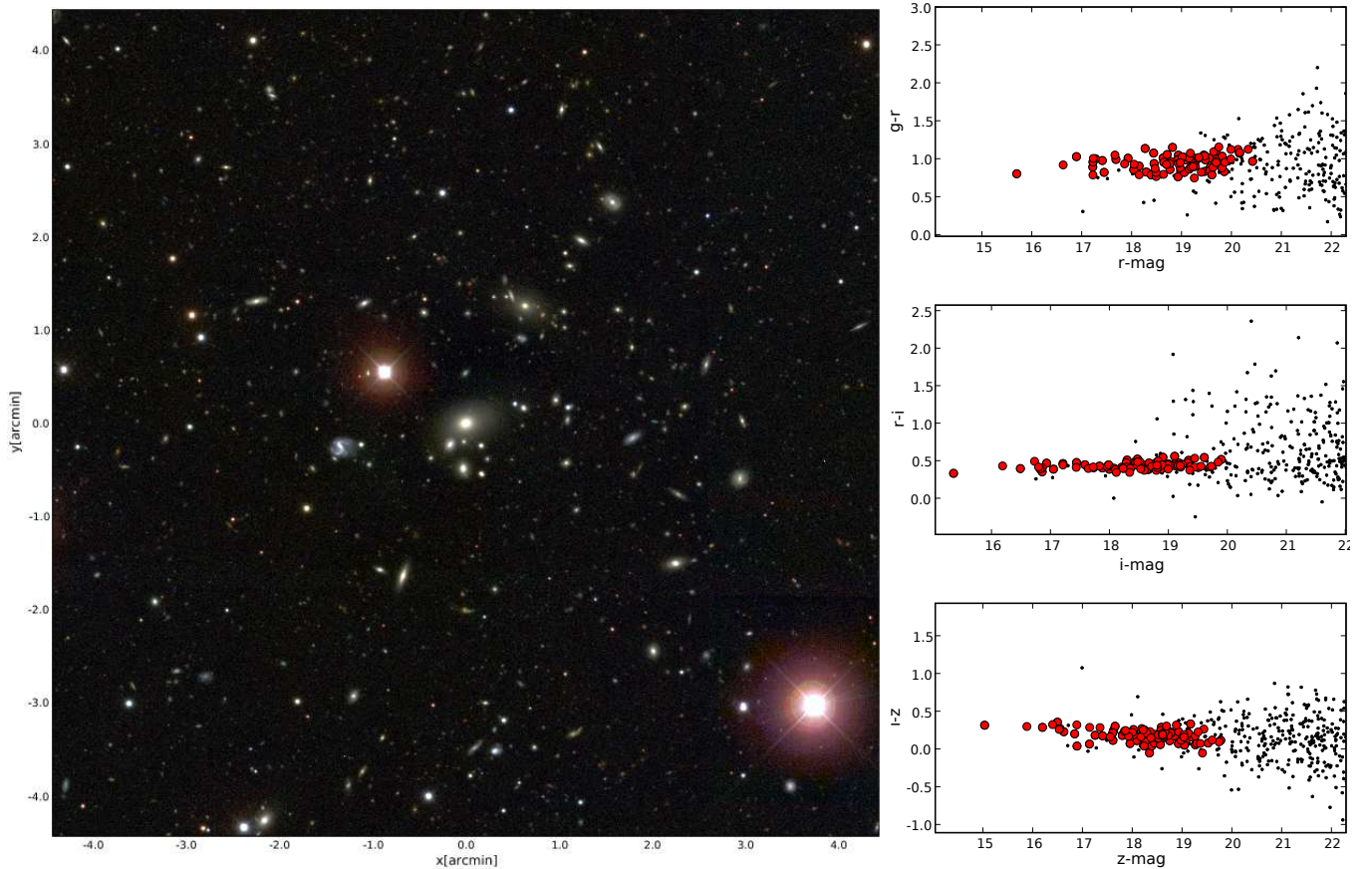


FIG. 6.— The composed *gri* color image (left panel) and color-magnitude relations (right) for X-ray cluster RXJ2325.6–5443 from Mullis et al. (2003). Red points represent galaxies classified as E/S0 by BPZ that satisfy the conditions to be cluster members as described in the main text. Black dots are non-member galaxies in a  $5'$  region near the cluster center.

of E/S0 galaxies within  $R_{200}$  with colors and luminosities that satisfy conditions (b) and (c) above. Similarly,  $L_{200}$  is the total rest-frame integrated *r*-band luminosity of all member galaxies included in  $N_{200}^{\text{gal}}$  in units of  $10^{10} h^{-2} L_{\odot}$  and  $L_{\text{BCG}}$  is the rest-frame *r*-band luminosity of the BCG.

In order to have reliable estimates of  $N_{\text{gal}}$  it is necessary to determine the galaxy background contamination and implement an appropriate background subtraction method. The lack of spectroscopic redshifts in our sample only allowed a statistical removal of unrelated field galaxies with similar colors and redshifts that were projected along the line of sight to each cluster. We assumed that the presence of a cluster at some redshift is independent of the field population seen in projection. Therefore we estimate the surface number density of ellipticals in an annulus surrounding the cluster (within  $R_{200} < r < 2R_{200}$ ) with  $\Delta z = 0.05$  and the same colors as the cluster members. We measure this background contribution around the outskirts of each cluster and obtain a corrected value  $N_{\text{gal}}$  which is used to compute  $R_{200}$  and then corresponding values of  $N_{200}^{\text{gal}}$  and  $L_{200}$ . The magnitude of the correction ranges between 15–20%. We will refer to the corrected values hereafter. Moreover as our analysis is based on a magnitude-limited sample it is worth considering the fraction of lower luminosity galaxies that will fall below our magnitude limit ( $i = 22.5$ ) at higher redshifts. As in Menanteau & Hughes (2009), if

we make the assumption that the cluster population is like that of the five clusters at  $z < 0.2$  in our sample (see Table 5) and  $M^*$  evolves passively, then we can compute the fraction of  $L_{200}$  missed for clusters at higher redshifts. We estimate that we are missing 4%, 13%, 29% and 38% of the cluster luminosity at  $z = 0.4, 0.5, 0.6$  and 0.7 respectively. Given the uncertainty in this correction factor, we do not include it in our quoted luminosity values for the higher redshift clusters. This means our cluster masses,  $M(L_{200})$ , are underestimated by roughly these factors.

### 3.2. Recovery of Known Clusters

The area covered by the BCS in the 23hr region is a virtual desert in terms of known clusters and spectroscopic redshifts for galaxies with  $z > 0.1$ . We found one catalogued X-ray selected cluster from the 160 deg<sup>2</sup> *ROSAT* survey (Mullis et al. 2003): RXJ2325.6–5443 at  $z = 0.102$  with an X-ray flux of  $F_X = 2.2 \times 10^{-13}$  erg cm<sup>-2</sup> s<sup>-1</sup> in the 0.5–2 keV band. Our cluster finding algorithm easily recovered this cluster and produced a photometric redshift estimate of  $\langle z \rangle = 0.10 \pm 0.02$ . Figure 6 shows the *gri* color composite optical image of the cluster as well as the color magnitude diagrams for cluster members. Using the techniques described below we estimate the mass of RXJ2325.6–5443 to be  $M(L_{200}) = 2.1 \times 10^{14}$  which is just below the detectability limit of ACT and therefore will not be included in our SZE predictions.

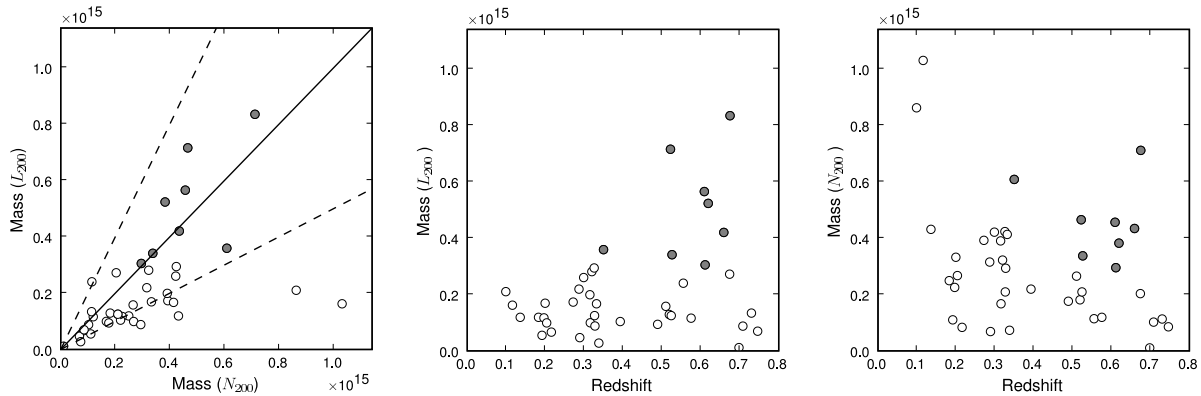


FIG. 7.— The mass observable parameters for the 38 clusters in our sample. Filled circles represent the eight new clusters above the mass limit  $M(L_{200}) > 3 \times 10^{14} M_{\odot}$ . The left panel shows the relation between the mass predictions using  $L_{200}$  vs.  $N_{200}^{\text{gal}}$  as the main parameter; the agreement is generally to within a factor of two, except for the nearest systems. The central and right panel show the mass estimates as a function of the cluster redshift using  $L_{200}$  and  $N_{200}^{\text{gal}}$  respectively, in units of solar mass.

From the  $M-T_X$  (Evrard et al. 1996) and  $L_X-T_X$  (Arnaud & Evrard 1999) relations we estimate a temperature of  $kT \sim 2.2$  keV and an X-ray flux of  $F_X \sim 5 \times 10^{-13}$  erg  $\text{cm}^{-2} \text{s}^{-1}$  (0.5–2 keV band) which is in rough agreement (factor of 2) with the published value. Considering the entire sample of 38 clusters, RXJ2325.6–5443 is the closest and, based on our estimated masses from the optical properties and the  $M-T_X$  and  $L_X-T_X$  relations, has the highest predicted X-ray flux of the sample. Still, even this value is below the X-ray detection threshold of the *ROSAT* All Sky Survey (RASS) and so, as expected, we find that none of our new optical clusters are significant RASS X-ray sources.

### 3.3. Cluster Mass Estimation

In this section we use the mass-richness relations based on  $N_{1\text{Mpc}}$  to weigh our new optical clusters. Both Johnston et al. (2007) and Reyes et al. (2008) found that the luminosity-mass and richness-mass relations were well described by power-law functions and they measured the normalizations and slopes in these relations using  $\chi^2$  minimization. Their values are in broad agreement, but we will use the fits provided by Reyes et al. (2008) since they restrict their fits to clusters with  $N_{200} > 10$  and give results for two redshift bins:  $0.10 < z < 0.23$  and  $0.23 < z < 0.30$ . It is important to note that our clusters go well beyond  $z = 0.3$  and that we extrapolate the relation in the last redshift bin for clusters with  $z > 0.3$ . We investigated the two fitting functions based on  $L_{200}$  and  $N_{200}^{\text{gal}}$  (see section 5.2.1 from Reyes et al. 2008 for full details), which are described as:

$$M(N_{200}, L_{\text{BCG}}) = M_N^0 (N_{200}/20)^{\alpha_N} (L_{\text{BCG}}/\bar{L}_{\text{BCG}}^{(N)})^{\gamma_N} \quad (7)$$

$$M(L_{200}, L_{\text{BCG}}) = M_L^0 (L_{200}/40)^{\alpha_L} (L_{\text{BCG}}/\bar{L}_{\text{BCG}}^{(L)})^{\gamma_L} \quad (8)$$

where  $M$  is the mass observational equivalent of  $M_{200\bar{\rho}}^{12}$  in units of  $10^{14} M_{\odot}$ ,  $L_{200}$  is in units of  $10^{10} h^{-2} L_{\odot}$  and the  $L_{\text{BCG}}$  dependence is normalized by its mean value.

<sup>12</sup>  $M_{200\bar{\rho}}$  is the halo mass enclosed within  $R_{200}$ , defined as a radius of spherical volume within which the mean density is 200 times the critical density.

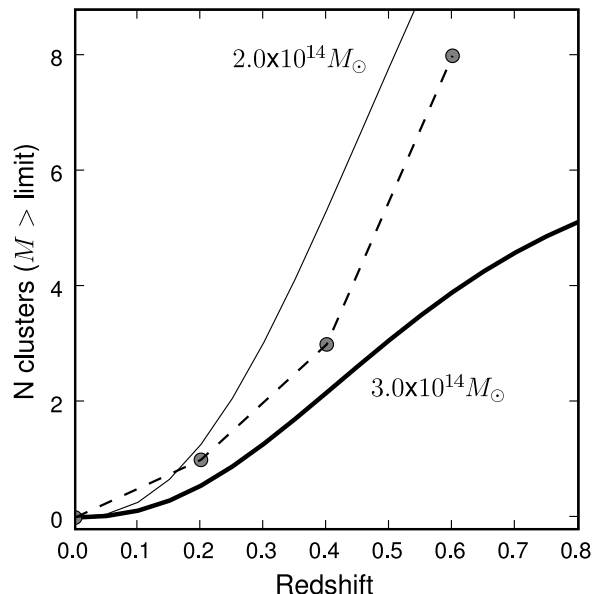


FIG. 8.— The gray circles show the total number of clusters with  $M(L_{200}) > 3 \times 10^{14} M_{\odot}$  observed in the  $\simeq 8 \text{ deg}^2$  region analyzed here. The thin and thick lines show the predicted number of clusters in the region for cluster masses greater than  $2 \times 10^{14} M_{\odot}$  and  $3 \times 10^{14} M_{\odot}$  respectively, using the WMAP 5-year best-fit cosmological model and the Jenkins et al. (2001) halo mass function.

This is also described by a power-law function for a given value of  $L_{200}$  and  $N_{200}^{\text{gal}}$ :

$$\bar{L}_{\text{BCG}}^{(N)} \equiv \bar{L}_{\text{BCG}}(N_{200}) = a_N N_{200}^{b_N} \quad (9)$$

$$\bar{L}_{\text{BCG}}^{(L)} \equiv \bar{L}_{\text{BCG}}(L_{200}) = a_L L_{200}^{b_L} \quad (10)$$

The published best-fitting parameters for  $M^0$ ,  $\alpha$  and  $\gamma$  in Eqs. (7) and (8) as well as the values of  $a$ ,  $b$  for Eqs. (9) and (10) are shown in Table 3. The combination of equations (7), (8) and (9), (10) for  $N_{200}^{\text{gal}}$  and  $L_{200}$  respectively enable us to obtain mass estimates for any cluster with  $N_{\text{gal}} > 10$ .



TABLE 3  
MASS-RICHNESS POWER-LAW FUNCTION BEST FITTING PARAMETERS

Redshift	$(10^{10}h^{-2}L_{\odot})$				$M_N^0$	$\alpha_N$	$\gamma_N$	$M_L^0$	$\alpha_L$	$\gamma_L$
	$a_N$	$a_L$	$b_N$	$b_L$						
$0.10 < z < 0.23$	1.54	7.77	0.41	0.67	$1.27 \pm 0.08$	$1.20 \pm 0.09$	$0.71 \pm 0.14$	$1.81 \pm 0.15$	$1.27 \pm 0.17$	$0.40 \pm 0.23$
$0.23 < z < 0.70$	1.64	7.92	0.43	0.66	$1.57 \pm 0.14$	$1.12 \pm 0.15$	$0.34 \pm 0.24$	$1.76 \pm 0.22$	$1.30 \pm 0.29$	$0.26 \pm 0.41$

The left panel of Fig. 7 compares the masses obtained using  $N_{200}$  and  $L_{200}$  for our 38 optical clusters. The solid line denotes equality between the estimates while the two dashed lines show a factor of 2 range. Most clusters fall within this range, establishing a lower bound on our mass error. The two most significant outliers correspond to nearby clusters (see the right panel of Fig. 7) for which  $N_{200}$  is evidently overpredicting the mass compared to  $L_{200}$ . In one of these cases (which is RXJ2325.6–5443), the mass inferred by  $N_{200}$  grossly overpredicts (by more than an order of magnitude) the estimated X-ray flux. The natural concentration of luminosities in clusters (i.e., that more luminous galaxies dominate the central regions of clusters) suggests that the mass estimate derived from  $L_{200}$  should be more robust than that from  $N_{200}$  as a function of redshift. For these reasons we use the cluster mass estimate derived from  $L_{200}$  in predicting the SZE signal. Hereafter we refer to this mass as  $M_{200}^L$ .

Table 4 displays the 8 clusters with  $M(L_{200}) > 3 \times 10^{14}M_{\odot}$  in the 8 square-degree sky area covered by our analysis. These clusters also have  $M(N_{200})$  above the same mass limit. In Figure 8 we show the cumulative number distribution of these clusters as a function of redshift, compared with expectations from simulations (H. Trac, private communication), using the mass function of dark matter haloes from Jenkins et al. (2001) and WMAP5 cosmology (Komatsu et al. 2008). The heavy solid curve shows expectations for a mass limit of  $3 \times 10^{14}M_{\odot}$ , while the light solid curve indicates a mass limit of  $2 \times 10^{14}M_{\odot}$ . This figure demonstrates that the number of clusters we observe is consistent with a mass limit in the range of  $2 - 3 \times 10^{14}M_{\odot}$ . In Table 5 we display the properties for the remaining clusters with  $M(L_{200}) < 3 \times 10^{14}M_{\odot}$ .

#### 4. PREDICTIONS OF THE SUNYAEV-ZEL'DOVICH EFFECT SIGNAL

Scaling relations between the integrated thermal SZE signal and cluster mass have emerged from current N-body plus hydrodynamic simulations of galaxy clusters. In this section we use these relations and our optically-derived mass estimates,  $M_{200}^L$ , to predict the SZE signal to be observed by ACT and SPT when these experiments survey this sky region.

The SZE signal consists of small distortions to the CMB spectrum originating from inverse Compton scattering by electrons in the hot plasma of clusters of galaxies (Sunyaev & Zeldovich 1980). Here we consider the thermal SZ flux  $Y$ , defined as the integrated Compton  $y$ -parameter,

$$Y = d_A^2(z) \int_{\Omega} y d\Omega = \frac{k_B \sigma_T}{m_e c^2} \int_V n_e T_e dV, \quad (11)$$

where  $n_e$  and  $T_e$  are the number density and temperature

of hot electrons in the cluster,  $m_e$  is electron rest mass,  $c$  is the speed of light,  $\sigma_T$  is the Thompson scattering cross section and  $d_A(z)$  is the angular diameter distance. The projected area,  $dA$ , and solid angle,  $d\Omega$ , are related by the angular diameter distance as  $dA = d_A^2(z)d\Omega$ .

Self-similar scaling relations (Kaiser 1986) predict that the virialized mass  $M$  in clusters scales with the gas temperature as  $M \propto T^{3/2}/E(z)$  where  $E(z) = (\Omega_m(1+z)^3 + \Omega_{\Lambda})^{1/2}$  for a flat cosmology. If clusters were isothermal, we would expect their SZE signal to scale like  $Y \propto f_{\text{gas}} M_{\text{halo}} T$  and therefore the self-similar SZ flux-mass scaling relation should have the shape  $Y \propto f_{\text{gas}} M^{5/3} E^{2/3}(z)$  where  $f_{\text{gas}}$  is the cluster mass fraction. However, clusters are not always isothermal or in hydrostatic equilibrium and physical processes like star formation and feedback will also contribute to deviations from self-similarity.

Prompted by the upcoming SZ surveys, several studies have characterized in detail the  $Y - M$  scaling relation using simple power-law fits to cosmological N-body simulations. Here we will use the recent  $Y - M$  fits from Sehgal et al. (2007), who included gas simulations employing small-scale cluster physics such as star formation and feedback into a large cosmological N-body simulation. From their catalog of  $\sim 10^5$  simulated clusters with  $M_{200} > 7.5 \times 10^{13}M_{\odot}$ , Sehgal et al. (2007) fit the relation

$$\frac{Y_{200}}{E(z)^{2/3}} = 10^{\beta} \left( \frac{M_{200}}{10^{14}M_{\odot}} \right)^{\alpha}, \quad (12)$$

where  $Y_{200}$  and  $M_{200}$  are the projected SZ Compton  $y$ -parameter and mass respectively in a disk of radius  $R_{200}$ . We use the best fit values  $\alpha = 1.876 \pm 0.005$  and  $\beta = -5.4774 \pm 0.0009$  for all clusters regardless of redshift, as the redshift dependence of the fits is very weak (see Table 2 from Sehgal et al. 2007). The power-law index that they report is slightly steeper than ones quoted by some previous hydrodynamic simulations (see Hernández-Monteagudo et al. 2006; Nagai 2006; Motl et al. 2005, for example), which Sehgal et al. (2007) attribute to their more realistic feedback prescription (i.e., including the effects of AGN and supernovae). We use the power-law model from equation 12 and the optical  $M_{200}^L$  mass estimates for our 8 new massive clusters to predict the integrated  $Y_{200}$  signal to be observed by ACT and SPT. Table 4 gives the results in physical units of  $\text{Mpc}^2$  and observable ones of  $\text{arcmin}^2$ .

#### 5. RESULTS AND CONCLUSIONS

In this article we have laid out the techniques and methods for our analysis of a large multi-band optical survey with the Blanco telescope and Mosaic-II instrument under the aegis of the Southern Cosmology Survey.

TABLE 4  
OPTICAL CLUSTERS WITH  $M(L_{200}) > 3 \times 10^{14} M_{\odot}$

ID	$z$	$N_{\text{gal}}$	$N_{200}^{\text{gal}}$	$L_{200}[L_{\odot}]$	$[M_{\odot}]$		$[M_{\text{pc}^2}]$	$[\text{arcmin}^2]$
					$M(N_{200})$	$M(L_{200})$	$Y_{200}/E(z)^{2/3}$	$Y_{200}$
SCSO J233430.2–543647.5	0.35	$32.1 \pm 5.8$	$43.8 \pm 7.0$	$1.8 \times 10^{12} \pm 2.9 \times 10^{10}$	$6.1 \times 10^{14}$	$3.6 \times 10^{14}$	$3.5 \times 10^{-05}$	$4.8 \times 10^{-04}$
SCSO J233556.8–560602.3	0.52	$31.4 \pm 5.9$	$33.5 \pm 6.4$	$3.3 \times 10^{12} \pm 1.4 \times 10^{11}$	$4.6 \times 10^{14}$	$7.2 \times 10^{14}$	$1.2 \times 10^{-04}$	$1.1 \times 10^{-03}$
SCSO J233425.6–542718.0	0.53	$26.1 \pm 5.4$	$26.9 \pm 5.6$	$1.8 \times 10^{12} \pm 9.5 \times 10^{10}$	$3.4 \times 10^{14}$	$3.4 \times 10^{14}$	$3.2 \times 10^{-05}$	$3.0 \times 10^{-04}$
SCSO J232211.0–561847.4	0.61	$31.1 \pm 5.7$	$34.1 \pm 6.1$	$2.8 \times 10^{12} \pm 1.1 \times 10^{11}$	$4.6 \times 10^{14}$	$5.6 \times 10^{14}$	$7.9 \times 10^{-05}$	$6.8 \times 10^{-04}$
SCSO J233731.7–560427.9	0.61	$25.6 \pm 5.4$	$23.1 \pm 5.3$	$1.7 \times 10^{12} \pm 1.7 \times 10^{11}$	$3.0 \times 10^{14}$	$3.0 \times 10^{14}$	$2.6 \times 10^{-05}$	$2.2 \times 10^{-04}$
SCSO J234012.6–541907.2	0.62	$22.7 \pm 5.2$	$24.9 \pm 5.4$	$2.4 \times 10^{12} \pm 1.4 \times 10^{11}$	$3.8 \times 10^{14}$	$5.2 \times 10^{14}$	$6.9 \times 10^{-05}$	$5.8 \times 10^{-04}$
SCSO J234004.9–544444.8	0.66	$30.7 \pm 5.8$	$37.5 \pm 6.7$	$2.3 \times 10^{12} \pm 2.4 \times 10^{11}$	$4.3 \times 10^{14}$	$4.2 \times 10^{14}$	$4.6 \times 10^{-05}$	$3.8 \times 10^{-04}$
SCSO J232829.7–544255.4	0.68	$74.6 \pm 8.7$	$65.7 \pm 9.7$	$4.4 \times 10^{12} \pm 4.3 \times 10^{11}$	$7.1 \times 10^{14}$	$8.3 \times 10^{14}$	$1.6 \times 10^{-04}$	$1.3 \times 10^{-03}$

NOTE. — Catalog of the optical clusters with mass estimates  $> 3 \times 10^{14} M_{\odot}$  from the  $M(L_{200})$  values. Each cluster's redshift is the mean photometric redshift computed using the elliptical in the center of the cluster. The ID is based on the position of the BCG.

TABLE 5  
OPTICAL CLUSTERS WITH  $M(L_{200}) < 3 \times 10^{14} M_{\odot}$

ID	$z$	$N_{\text{gal}}$	$N_{200}^{\text{gal}}$	$L_{200}[L_{\odot}]$	$[M_{\odot}]$	
					$M(N_{200})$	$M(L_{200})$
SCSO J232540.2–544430.9	0.10	$123.9 \pm 11.2$	$278.1 \pm 18.5$	$3.3 \times 10^{12} \pm 2.8 \times 10^{10}$	$8.6 \times 10^{14}$	$2.1 \times 10^{14}$
SCSO J232230.9–541608.3	0.12	$69.5 \pm 8.4$	$145.3 \pm 12.8$	$1.7 \times 10^{12} \pm 1.1 \times 10^{10}$	$1.0 \times 10^{15}$	$1.6 \times 10^{14}$
SCSO J233000.4–543707.7	0.14	$38.0 \pm 6.4$	$39.0 \pm 7.2$	$1.0 \times 10^{12} \pm 1.0 \times 10^{10}$	$4.3 \times 10^{14}$	$1.2 \times 10^{14}$
SCSO J232419.6–552548.9	0.18	$39.3 \pm 6.5$	$36.9 \pm 7.0$	$1.4 \times 10^{12} \pm 1.8 \times 10^{10}$	$2.5 \times 10^{14}$	$1.2 \times 10^{14}$
SCSO J233106.9–555119.5	0.19	$26.3 \pm 5.5$	$35.3 \pm 6.4$	$9.7 \times 10^{11} \pm 2.9 \times 10^{10}$	$1.1 \times 10^{14}$	$5.5 \times 10^{13}$
SCSO J233252.9–561454.1	0.20	$34.0 \pm 6.1$	$43.4 \pm 7.2$	$1.5 \times 10^{12} \pm 2.2 \times 10^{10}$	$2.2 \times 10^{14}$	$1.2 \times 10^{14}$
SCSO J233215.5–544211.6	0.20	$43.5 \pm 6.8$	$42.6 \pm 7.6$	$1.8 \times 10^{12} \pm 3.4 \times 10^{10}$	$3.3 \times 10^{14}$	$1.7 \times 10^{14}$
SCSO J233037.1–554338.8	0.20	$27.5 \pm 5.6$	$35.2 \pm 6.4$	$1.1 \times 10^{12} \pm 1.7 \times 10^{10}$	$2.7 \times 10^{14}$	$9.9 \times 10^{13}$
SCSO J233550.6–552820.4	0.22	$14.5 \pm 4.4$	$10.6 \pm 3.5$	$7.4 \times 10^{11} \pm 2.2 \times 10^{10}$	$8.3 \times 10^{13}$	$6.6 \times 10^{13}$
SCSO J232200.4–544459.7	0.27	$34.6 \pm 6.0$	$41.0 \pm 6.9$	$1.2 \times 10^{12} \pm 1.8 \times 10^{10}$	$3.9 \times 10^{14}$	$1.7 \times 10^{14}$
SCSO J233522.6–553237.0	0.29	$31.4 \pm 5.9$	$32.1 \pm 6.3$	$1.5 \times 10^{12} \pm 2.4 \times 10^{10}$	$3.2 \times 10^{14}$	$2.2 \times 10^{14}$
SCSO J233807.5–560304.9	0.30	$32.0 \pm 5.9$	$37.7 \pm 6.6$	$1.6 \times 10^{12} \pm 3.2 \times 10^{10}$	$4.2 \times 10^{14}$	$2.6 \times 10^{14}$
SCSO J232956.0–560808.3	0.32	$39.6 \pm 6.5$	$37.0 \pm 6.7$	$1.3 \times 10^{12} \pm 2.3 \times 10^{10}$	$3.9 \times 10^{14}$	$2.0 \times 10^{14}$
SCSO J232839.5–551353.8	0.32	$40.3 \pm 6.5$	$18.9 \pm 5.2$	$7.9 \times 10^{11} \pm 2.2 \times 10^{10}$	$1.7 \times 10^{14}$	$1.0 \times 10^{14}$
SCSO J232633.6–550111.5	0.32	$74.3 \pm 8.7$	$35.2 \pm 7.4$	$1.9 \times 10^{12} \pm 4.5 \times 10^{10}$	$3.2 \times 10^{14}$	$2.8 \times 10^{14}$
SCSO J233753.8–561147.6	0.33	$33.2 \pm 5.9$	$41.3 \pm 6.7$	$1.8 \times 10^{12} \pm 3.3 \times 10^{10}$	$4.2 \times 10^{14}$	$2.9 \times 10^{14}$
SCSO J232156.4–541428.8	0.33	$20.1 \pm 4.8$	$19.9 \pm 4.7$	$8.6 \times 10^{11} \pm 1.0 \times 10^{10}$	$2.1 \times 10^{14}$	$1.2 \times 10^{14}$
SCSO J233003.6–541426.7	0.33	$29.6 \pm 5.7$	$30.4 \pm 5.9$	$6.6 \times 10^{11} \pm 1.8 \times 10^{10}$	$2.9 \times 10^{14}$	$8.8 \times 10^{13}$
SCSO J233231.4–540135.8	0.33	$45.9 \pm 6.9$	$42.7 \pm 7.1$	$1.2 \times 10^{12} \pm 2.2 \times 10^{10}$	$4.1 \times 10^{14}$	$1.7 \times 10^{14}$
SCSO J233110.6–555213.5	0.39	$21.1 \pm 4.9$	$20.8 \pm 4.9$	$7.3 \times 10^{11} \pm 1.7 \times 10^{10}$	$2.2 \times 10^{14}$	$1.0 \times 10^{14}$
SCSO J233618.3–555440.3	0.49	$17.4 \pm 4.6$	$15.3 \pm 4.2$	$6.3 \times 10^{11} \pm 3.6 \times 10^{10}$	$1.8 \times 10^{14}$	$9.4 \times 10^{13}$
SCSO J233706.3–541903.8	0.51	$25.5 \pm 5.3$	$29.9 \pm 5.9$	$1.2 \times 10^{12} \pm 8.5 \times 10^{10}$	$2.6 \times 10^{14}$	$1.6 \times 10^{14}$
SCSO J233816.9–555331.1	0.52	$19.8 \pm 4.7$	$19.8 \pm 4.7$	$9.7 \times 10^{11} \pm 3.4 \times 10^{10}$	$1.8 \times 10^{14}$	$1.3 \times 10^{14}$
SCSO J232619.8–552308.8	0.52	$18.8 \pm 4.7$	$18.2 \pm 4.5$	$8.1 \times 10^{11} \pm 6.1 \times 10^{10}$	$2.1 \times 10^{14}$	$1.2 \times 10^{14}$
SCSO J232215.9–555045.6	0.56	$11.0 \pm 4.0$	$7.4 \pm 2.9$	$1.2 \times 10^{12} \pm 6.1 \times 10^{10}$	$1.1 \times 10^{14}$	$2.4 \times 10^{14}$
SCSO J232247.6–541110.1	0.57	$14.9 \pm 4.3$	$11.5 \pm 3.6$	$8.2 \times 10^{11} \pm 4.3 \times 10^{10}$	$1.2 \times 10^{14}$	$1.2 \times 10^{14}$
SCSO J232342.3–551915.1	0.67	$18.1 \pm 4.7$	$18.5 \pm 4.6$	$1.7 \times 10^{12} \pm 1.5 \times 10^{11}$	$2.0 \times 10^{14}$	$2.7 \times 10^{14}$
SCSO J233403.7–555250.7	0.71	$11.5 \pm 4.1$	$10.0 \pm 3.3$	$6.5 \times 10^{11} \pm 1.5 \times 10^{11}$	$1.0 \times 10^{14}$	$8.8 \times 10^{13}$
SCSO J233951.1–551331.3	0.73	$11.6 \pm 3.9$	$9.9 \pm 3.3$	$8.8 \times 10^{11} \pm 1.8 \times 10^{11}$	$1.1 \times 10^{14}$	$1.3 \times 10^{14}$
SCSO J233720.2–562115.1	0.75	$10.7 \pm 4.0$	$7.7 \pm 2.9$	$5.0 \times 10^{11} \pm 1.2 \times 10^{11}$	$8.5 \times 10^{13}$	$7.0 \times 10^{13}$

NOTE. — Catalog of the optical clusters with mass estimates  $< 3 \times 10^{14} M_{\odot}$  from the  $M(L_{200})$  values. Each cluster's redshift is the mean photometric redshift computed using the elliptical in the center of the cluster. The ID is based on the position of the BCG.

We have obtained sub-arcsecond astrometric precision and sufficient photometric accuracy for the estimation of redshifts to  $\delta z < 0.1$ . Forty-two optical cluster candidates were identified from an area of the sky covering  $\simeq 8 \text{ deg}^2$ ; the richness and integrated galaxy luminosity of the clusters were measured. Based on correlations between these optical observables and cluster mass as established by SDSS cluster surveys (Johnston et al. 2007;

Reyes et al. 2008) we provide mass estimates (in addition to positions and redshifts) for 8 new clusters whose inferred masses lie above  $3 \times 10^{14} M_{\odot}$ . These clusters are all likely to be detected by ACT and SPT if these experiments reach their expected sensitivity levels. Although the uncertainties on the estimated mass and inferred SZE signal are large (factors of 2 or so), the accuracy of our cluster positions and redshifts are quite good and typical

for 4-band imaging survey data. Moreover, it is worth noting that the  $Y - M$  relation varies quite a bit from simulation to simulation (differences of a factor of 2 in  $M$  at fixed  $Y$ ), so our predicted masses are well within the uncertainty range of the latest theoretical predictions. In an effort to reduce the mass errors we have begun to estimate weak lensing masses from the current Blanco data (McInnes et al. 2009). We also note that significant additional areas of the BCS are now publicly available and will be presented in future publications.

The strength of the SCS is its multi-wavelength aspect and large sky area coverage. The 23hr region of the sky analyzed here has now been surveyed in the UV by GALEX and in the X-ray band by *XMM-Newton*; over the next several months as these data become available, we will incorporate them into the SCS. Correlation analyses of these multi-wavelength data should allow us to reduce the large errors on inferred cluster masses and study the cluster selection biases across wavebands. Secure confirmation of all candidates, as well as additional mass constraints, rest on follow-up optical spectroscopy, which we are pursuing at the Southern African Large Telescope and elsewhere. Finally, once ACT and SPT

data become available, the rich optical data set analyzed here will be a valuable source for understanding and quantifying the impact of large scale structure on secondary anisotropies in the CMB.

FM would like to thank Txitxo Benitez for discussions and the use of BPZ priors and templates. JPH would like to thank Kent Patterson for help during the early phases of this project and the Aresty Center for Undergraduate Research at Rutgers for financial support. AK has been supported by NSF grant AST-0546035. LI thanks Centro de Astrofisica Fondap. We thank Armin Rest and Frank Valdes for helpful discussion on the image analysis and we also acknowledge David Spergel for several important insights and suggestions. We are thankful to Wayne Barkhouse, Mark Brodwin, Will High, Yen-Ting Lin and the entire BCS team for the careful planning and execution of the NOAO observations on which this paper is based. Financial support was provided by the NASA LTSA program (grant number NAG5-11714) and the National Science Foundation under the PIRE program (award number OISE-0530095).

## REFERENCES

- Arnaud, M., & Evrard, A. E. 1999, *MNRAS*, 305, 631  
 Benítez, N. 2000, *ApJ*, 536, 571  
 Benítez, N., et al. 2004, *ApJS*, 150, 1  
 Bertin, E., & Arnouts, S. 1996, *A&AS*, 117, 393  
 Bertin, E., SWarp Resample and Coadd Software, <http://terapix.iap.fr/cpltd/oldSite/soft/swarp/index.html>  
 Bhattacharya, S., Di Matteo, T., & Kosowsky, A. 2007, *ArXiv e-prints*, 710, arXiv:0710.5574  
 Birkinshaw, M., Hughes, J. P., & Arnaud, K. A. 1991, *ApJ*, 379, 466  
 Bonamente, M., Joy, M. K., LaRoque, S. J., Carlstrom, J. E., Reese, E. D., & Dawson, K. S. 2006, *ApJ*, 647, 25  
 Böhringer, H., et al. 2001, *A&A*, 369, 826  
 Brown, M. J. I., Dey, A., Jannuzi, B. T., Brand, K., Benson, A. J., Brodwin, M., Croton, D. J., & Eisenhardt, P. R. 2007, *ApJ*, 654, 858  
 Carlstrom, J. E., Holder, G. P., & Reese, E. D. 2002, *ARA&A*, 40, 643  
 Cross, N. J. G., et al. 2004, *AJ*, 128, 1990  
 Ebeling, H., Edge, A. C., Bohringer, H., Allen, S. W., Crawford, C. S., Fabian, A. C., Voges, W., & Huchra, J. P. 1998, *MNRAS*, 301, 881  
 Eisenhardt, P. R. M., et al. 2008, *ArXiv e-prints*, 804, arXiv:0804.4798  
 Evrard, A. E., Metzler, C. A., & Navarro, J. F. 1996, *ApJ*, 469, 494  
 Fowler, J. W., et al. 2007, *Appl. Opt.*, 46, 3444  
 Gal, R. R., de Carvalho, R. R., Odewahn, S. C., Djorgovski, S. G., & Margoniner, V. E. 2000, *AJ*, 119, 12  
 Gal, R. R., de Carvalho, R. R., Lopes, P. A. A., Djorgovski, S. G., Brunner, R. J., Mahabal, A., & Odewahn, S. C. 2003, *AJ*, 125, 2064  
 Gal, R. R., Lopes, P. A. A., de Carvalho, R. R., Kohl-Moreira, J. L., Capelato, H. V., & Djorgovski, S. G. 2009, *AJ*, 137, 2981  
 Génova-Santos, R., et al. 2005, *MNRAS*, 363, 79  
 Génova-Santos, R., et al. 2008, *ArXiv e-prints*, 804, arXiv:0804.0199  
 Gladders, M. D., & Yee, H. K. C. 2005, *ApJS*, 157, 1  
 Gómez, P. L., et al. 2003, *Astronomical Society of the Pacific Conference Series*, 301, 495  
 Halverson, N. W., et al. 2008, *ArXiv e-prints*, 807, arXiv:0807.4208  
 Hansen, S. M., McKay, T. A., Wechsler, R. H., Annis, J., Sheldon, E. S., & Kimball, A. 2005, *ApJ*, 633, 122  
 Herbig, T., Lawrence, C. R., Readhead, A. C. S., & Gulkis, S. 1995, *ApJ*, 449, L5  
 Hernández-Monteagudo, C., Génova-Santos, R., & Atrio-Barandela, F. 2004, *ApJ*, 613, L89  
 Hernández-Monteagudo, C., Trac, H., Verde, L., & Jimenez, R. 2006, *ApJ*, 652, L1  
 Infante, L. 1994, *A&A*, 282, 353  
 Jenkins, A., Frenk, C. S., White, S. D. M., Colberg, J. M., Cole, S., Evrard, A. E., Couchman, H. M. P., & Yoshida, N. 2001, *MNRAS*, 321, 372  
 Johnston, D. E., et al. 2007, *ArXiv e-prints*, 709, arXiv:0709.1159  
 Jones, M., et al. 1993, *Nature*, 365, 320  
 Kaiser, N. 1986, *MNRAS*, 222, 323  
 Komatsu, E., et al. 2008, *ArXiv e-prints*, 803, arXiv:0803.0547  
 Koester, B. P., et al. 2007, *ApJ*, 660, 239  
 Kosowsky, A. 2006, *New Astronomy Reviews*, 50, 969  
 Kravtsov, A. V., Berlind, A. A., Wechsler, R. H., Klypin, A. A., Gottlöber, S., Allgood, B., & Primack, J. R. 2004, *ApJ*, 609, 35  
 Lubin, L. M., & Postman, M. 1996, *AJ*, 111, 1795  
 Mandelbrot, B. 1975, *Academie des Sciences Paris Comptes Rendus Serie Sciences Mathematiques*, 280, 1551  
 McInnes, R. N., Menanteau, F., Heavens, A. F., Hughes, J. P., Jimenez, R., Massey, R., Simon, P., & Taylor, A. N. 2009, arXiv:0903.4410  
 Menanteau, F., & Hughes, J. P. 2009, *ApJ*, 694, L136  
 Mobasher, B., et al. 2004, *ApJ*, 600, L167  
 Motl, P. M., Hallman, E. J., Burns, J. O., & Norman, M. L. 2005, *ApJ*, 623, L63  
 Mullis, C. R., et al. 2003, *ApJ*, 594, 154  
 Mullis, C. R., Rosati, P., Lamer, G., Böhringer, H., Schwöpe, A., Schuecker, P., & Fassbender, R. 2005, *ApJ*, 623, L85  
 Nagai, D. 2006, *ApJ*, 650, 538  
 Niemack, M. D., Jimenez, R., Verde, L., Menanteau, F., Panter, B., & Spergel, D. 2008, *ArXiv e-prints*, 803, arXiv:0803.3221  
 Postman, M., Lubin, L. M., Gunn, J. E., Oke, J. B., Hoessel, J. G., Schneider, D. P., & Christensen, J. A. 1996, *AJ*, 111, 615  
 Postman, M., Lauer, T. R., Oegerle, W., & Donahue, M. 2002, *ApJ*, 579, 93  
 Postman, M., Lubin, L. M., & Oke, J. B. 2001, *AJ*, 122, 1125  
 Reese, E. D., et al. 2000, *ApJ*, 533, 38  
 Reyes, R., Mandelbaum, R., Hirata, C., Bahcall, N., & Seljak, U. 2008, *MNRAS*, 390, 1157  
 Ruhl, J., et al. 2004, *Proc. SPIE*, 5498, 11  
 Schechter, P. 1976, *ApJ*, 203, 297  
 Sehgal, N., Trac, H., Huffenberger, K., & Bode, P. 2007, *ApJ*, 664, 149  
 Smith, J. A., Allam, S. S., Tucker, D. L., Stute, J. L., Rodgers, C. T., & Stoughton, C. 2007, *AJ*, submitted  
 Staniszewski, Z., et al. 2008, arXiv:0810.1578  
 Sunyaev, R. A., & Zeldovich, Y. B. 1980, *ARA&A*, 18, 537

- Valdes, F. G. 1998, *Astronomical Data Analysis Software and Systems VII*, 145, 53
- Yasuda, N., et al. 2001, *AJ*, 122, 1104